Interfacial Electronic Structure Engineering on Molybdenum Sulfide for Robust Dual-pH Hydrogen Evolution

Mingqiang Liu
Harbin Institute of Technology
Jia-ao Wang
University of Texas at Austin, USA
Gui-Gen Wang
Harbin Institute of Technology https://orcid.org/0000-0001-8606-8986
Fei Li
Harbin Institute of Technology
Ya-Wei Cai
Harbin Institute of Technology
Fuchun Zhang
Yan'an University
Jie Yu
Harbin Institute of Technology, Shenzhen https://orcid.org/0000-0003-2051-9689
Ya Yang (yayang@binn.cas.cn)
Beijing Institute of Nanoenergy and Nanosystems, Chinese Academy of Sciences
https://orcid.org/0000-0003-0168-2974

Article

Keywords: Molybdenum disulfide, Hydrogen evolution reaction, Surface electronic structure, Hetero geneous-phase-interface

Posted Date: March 24th, 2021

DOI: https://doi.org/10.21203/rs.3.rs-319079/v1

Version of Record: A version of this preprint was published at Nature Communications on September 6th, 2021. See the published version at https://doi.org/10.1038/s41467-021-25647-8.

Abstract

Molybdenum disulfide, as an electronic highly-adjustable catalysts material, tuning its electronic structure is crucial to enhance its intrinsic hydrogen evolution reaction (HER) activity. Nevertheless, there are yet huge challenges to the understanding and regulation of the surface electronic structure of molybdenum disulfide-based catalysts. Here we address these challenges by tuning its electronic structure of phase modulation synergistic with interfacial chemistry and defects from phosphorus or sulfur implantation, and we then successfully design and synthesize electrocatalysts with the multi-heterojunction interfaces (e.g., $1T_{0.81}$-MoS_2@Ni_2P), demonstrating superior HER activities and good stabilities with a small overpotentials of 38.9 and 98.5 mV at 10 mA/cm^2, a low Tafel slopes of 41 and 42 mV/dec in acidic as well as alkaline surroundings, outperforming commercial Pt/C catalyst and other reported Mo-based catalysts. Theoretical calculation verified that the incorporation of metallic-phase and intrinsic HER-active Ni-based materials into molybdenum disulfide could effectively regulate its electronic structure for making the bandgap narrower. Additionally, reduced nickel possesses empty orbitals, which is helpful for additional H binding ability. All these factors can decrease Mo-H bond strength, greatly improving the HER catalytic activity of these materials.

Introduction

Extensive use and depletion of fossil fuels resulting in serious pollution. Therefore, green and renewable fuel resources are required for continuing sustainable economic development.[1-3] Electrocatalysis acts as a vital role in the conversion of clean energy to achieve a sustainable approach to various commercial processes, including HER.[4,5] However, electrochemical water splitting is hindered by the large kinetic barrier and slow kinetics.[6-9] Pt-based electrocatalysts are recognized as highly efficient electrocatalysts due to good electrical conductivity,[10] fast kinetics, and the preference to overcome the large kinetic energy barrier involved in the above-mentioned process.[11] Unfortunately, high price and not desirable stability hinder the extended Pt-based catalysts' application.[12] Thus, it is very urgent to develop cost-effective Pt-free electrocatalysts with comparable activity and better stability.

Researchers recently have designed a wide range of low-cost catalysts, including transition-metal chalcogenides (TMDCs),[13,14] metal nitrides,[15,16] metal carbides,[17,18] and metal phosphides.[19,20] Among these candidates, MoS_2, a typical layered 2D TMDCs formed by Van der Waals interaction and stacking of S-Mo-S layers, attracts extensive interests with its adjustable bandgap, unique band structure, high energy-conversion efficiency, and earth abundance.[21-23] However, the electrocatalytic activity of MoS_2 is closely associated with its surface electric structure, such as phase structure or phase composition, interface active site, and defect. Interestingly, two main phases of MoS_2 were widely justified: 2H and 1T phases.[24] 2H phase has the most thermodynamical stability among the molybdenum sulfide family, whose HER activities are restrained by the amount and active site types as well as conductivity. Unlike the 2H phase, 1T phase one demonstrates higher catalytic activity since it has numerous active sites on the edges and a fast transfer rate. However, it is remaining a giant challenge of directly synthesizing the high

percentage 1T phase molybdenum sulfide due to the thermodynamic instability of $1T_{phase}$-MoS_2.[25] To solve this problem, a feasible strategy is to efficiently realize the 2H → 1T phase transformation to improve HER capability. Wang et al. found that a partial 2H → 1T MoS_2 phase transition by facile one-pot annealing of a large amount of $2H_{phase}$-MoS_2 under phosphorus vapor is able to enhance HER catalytic activities.[26] A synergistic strategy of doping nitrogen and intercalating PO_4^{3-} is reported, which can convert 2H- to 1T-phase with a conversion rate of up to 41%, and has excellent HER performance.[27] However, the electronic transport capacity and phase stability of the phase boundary of a single component (pure 1T-phase) are generally poor. In order to overcome the puzzles, the HER activity of the pure phase can be improved by constructing a heterogeneous boundary. Therefore, it is expected to further enhance the HER performance and its stability of traditional single 1T-phase or 2H-phase interface by constructing a composite heterojunction between 1T-phase and the other phases.[28]

Interface modification could be an effective approach to construct a composite heterojunction.[29,30] Ni-based materials (such as Ni_2P, NiS_2, Ni_2S_3, etc.) with high activity and conductivity have been considered as highly efficient electrocatalysis materials for HER,[19,20,31] as another heterogeneous interface, which is also very important to control the electronic structure of the MoS_2 interface. Kim et al. reported that Ni_2P nanoparticles were used to activate the MoS_2 base surface, which exhibits Pt-like HER performance in 0.5 M HCl solution.[31] Because the electronic structure of Ni_2P is a P62m space group, which could facilitate recombination at the atomic scale. Moreover, Ni has a unique α and β orbital integral asymmetric d orbital, which makes it easy for the lone pair of electrons to recombine with the d orbital of the exposed Mo atom on MoS_2 to generate new interface electrons, thereby improving HER performance. Lin et al. reported that a defect-rich heterogeneous interfacial catalyst (MoS_2/NiS_2) could provide abundant active sites to promote electron transfer, thereby further rapidly promoting electrocatalytic hydrogen evolution.[32] More importantly, the introduction of NiS_2 hybridization on the surface of MoS_2 generates new form of interface electrons, and $Ni^{\delta+}$ is reduced to low-valence Ni to improve the binding energy with hydrogen elements, thereby weakening the Mo-H strength. To sum up, although the heterojunction-phase catalyst synthesized by the above-mentioned approach further improves the HER activity and good stability, the understanding and regulation of the surface electronic structure on the MoS_2 interface are still huge challenges, and thus it is very necessary to develop an efficient synthesis approach to obtain stable multi-heterogeneous interface catalyst.

Here, we address these challenges by tuning its electronic structure through phase modulation synergistic with interfacial chemistry and defects of phosphorus or sulfur implantation, and we then successfully design and prepare a series of heterojunction-phase-interface electrocatalysts (denoted $1T_{0.81}$-MoS_2@Ni_2P and $1T_{0.72}$-MoS_2@NiS_2) with an outstanding HER activity and are stable in dual-pH surroundings. The strategies to control the electronic characteristics of the MoS_2 surface include surface phase modulation, surface defects, and the construction of hetero-structure (**Fig. 1a**). Furthermore, we control the hydrogen and hydroxyl adsorption energy through the synergistic effect of heterojunction-phase-interface catalysts (**Fig. 1b** and **Fig. 1c-f**) because the energy of the hydroxyl species is very

important for the hydrolysis accelerator. Starting from hydrothermally synthesized MoS_2 nanosheets, we develop a simple surface electronic structure modulation strategy of constructing multi-heterogeneous-phase-interface $1T_{0.81}$-MoS_2@Ni_2P and $1T_{0.72}$-MoS_2@NiS_2 electrocatalysts (**Fig. 1a**) by citric acid-induced hydrothermal synthesis, electrodeposition and then phosphorus (or sulfur) vapor thermal treatment approach for the first time. Our approach can not only realize the construction of abundant catalytic reactive sites but also improve the conversion rate of 2H to 1T (81%), and it is also convenient to introduce Ni_2P or NiS_2 heterogeneous interfaces. As to the surface electronic structure of catalysts, high-resolution transmission electron microscopy (HRTEM) images show that such phase-structures, heterojunction-phase-interface edges, and defects are derived by the featured electronic states and Ni atomic coordination. Additionally, X-ray photoelectron spectra (XPS) showed that citric acid induces hydrothermal synthesis of stable $1T_{0.41}$-MoS_2 (41% of 1T phase), and the $1T_{0.81}$-MoS_2 or $1T_{0.72}$-MoS_2 (81% or 72% of 1T phase) conversion rate is further improved after phosphorus or sulfur vapor thermal treatment. Electrodes containing $1T_{0.81}$-MoS_2@Ni_2P (or $1T_{0.72}$-MoS_2@NiS_2) only require 38.9 (or 186) and 98.5 mV (or 128) to achieve HER current density equal to 10 mA/cm^2. They also need Tafel slopes equal to 41 (or 79) and 42 (or 68) mV/dec in 1M H^+ or OH^- media, good stability during testing for 16 h in both media, respectively. The $1T_{0.81}$-MoS_2@Ni_2P (or $1T_{0.72}$-MoS_2@NiS_2) catalysts exhibited superior activities with Tafel slope values and the over-potentials lower than the values reported for Mo-base HER catalysts in both alkaline and acidic media.[25,26,28,31-34] The mechanism of hydrogen formation at the heterogeneous interface was elucidated by DFT calculation, which is attributed to the shortened bandgap, the decreased Mo-H bond strength, and the reduced electron cloud density around Ni providing enough empty d-orbitals to bind with H atoms. This work provides useful insights for exploring the enhancement mechanisms of HER with an optimized surface electronic structure on the MoS_2 interface, which provides an effective insight of constructing invaluable metal electrocatalysts for HER and other fields.

Results

Preparation and characterizations of multi-heterojunction interface electrocatalysts. The formation process of multi-heterojunction interface electrocatalysts is schematically illustrated in **Fig 1g**. $1T_{0.81}$-MoS_2@Ni_2P and $1T_{0.72}$-MoS_2@NiS_2 catalysts were synthesized by a three-step procedure. First, $1T_{0.41}$-MoS_2 catalyst was obtained on carbon cloth (CC) by acid-induced hydrothermal approach at 200 ^oC for 12 h (see details in "**Methods**" section). The as-obtained $1T_{0.41}$-MoS_2 catalyst shows a large number of microspheres (**Supplementary Fig. 1b-d**) with a narrow diameter distribution of 2.0 ~ 4.0 μm distributed uniformly on the surface of CC substrate. Flower-shaped MoS_2 microspheres are consisted of many aligned $1T_{0.41}$-MoS_2 nanosheets, on which the $Ni(OH)_2$ nanoparticles were then electro-deposited (see details in "**Methods**" section). $1T_{0.41}$-MoS_2@$Ni(OH)_2$ material inherited its morphology from spherical MoS_2. Subsequently, $1T_{0.41}$-MoS_2@$Ni(OH)_2$ material was loaded into a quartz tube mixed with red phosphorus or sulfur powder and sealed by oxyacetylene flame. Finally, these were heated to 600 ^oC for the reaction with red phosphorus or sulfur to synthesize $1T_{0.81}$-MoS_2@Ni_2P and $1T_{0.72}$-MoS_2@NiS_2

catalysts, respectively (**Supplementary Fig. 2, 3**). As to $1T_{0.81}$-MoS_2@Ni_2P catalyst, the MoS_2 microspheres are very rough, on which there distributes many random Ni_2P nanoparticles (**Supplementary Fig. 3**). It is because that the 1T/2H mixed-phase and heterojunction-interface structure reduces the adhesion of the gas-solid interface and facilitates releasing hydrogen from the catalyst surface, which is essential for enhancing HER.[29]

Next, the phase composition and crystal properties of $1T_{0.81}$-MoS_2@Ni_2P and $1T_{0.72}$-MoS_2@NiS_2 were obtained by X-ray diffraction (XRD) and Raman spectroscopy. There are some obvious characteristic diffraction peaks of 14.3°, 33.4°, and 59.2° (**Supplementary Fig. 4a**), which can be ascribed to $2H_{phase}$-MoS_2 according to the JCPDS card number #37-1429. However, the XRD peak of $1T_{0.81}$-MoS_2@Ni_2P and $1T_{0.72}$-MoS_2@NiS_2 located at $2\theta \approx 28.8°$ can be indexed as the (004) peak of $1T_{phase}$-MoS_2, which indicates that 1T- and 2H-mixed phases were successfully hydrothermally synthesized.[35] The other characteristic peaks ($2\theta \approx 31.3°$, 35.2°, 38.8°, 44.9°, and 53.3°) demonstrate that the $1T_{0.72}$-MoS_2@NiS_2 is a hybrid of NiS_2 (JCPDS#11-0099), which verifies the presence of NiS_2 nanoparticles. Similarly, as to $1T_{0.81}$-MoS_2@Ni_2P catalyst, its XRD results also showed the presence of Ni_2P nanoparticles (JCPDS#21-0590) on the $1T_{0.41}$-MoS_2 surface. Raman spectroscopy showed E_{2g}^1 and A_{1g} vibrational bands at 376.2 and 402.9 cm^{-1} peaks typical for $2H_{phase}$-MoS_2.[36] J_1, J_2 and J_3 vibrations at 147.3, 235.4 and 335.2 cm^{-1} are characteristic for $1T_{phase}$-MoS_2[37] (**Supplementary Fig. 4b**). These results prove that the 1T phase of MoS_2 is formed by the hydrothermal reaction induced by organic acids (e.g., citric acid).[35] $1T_{0.72}$-MoS_2@NiS_2 or $1T_{0.81}$-MoS_2@Ni_2P demonstrated three characteristic peaks of $1T_{phase}$-MoS_2 and the two characteristic peaks (E_{2g}^1 and A_{1g}) of $2H_{phase}$-MoS_2. Additionally, they showed a vibrational peak (437.3 cm^{-1}) of Ni-S[32] or three vibrational peaks (216.2 cm^{-1}, 249.7 cm^{-1}, and 269.5 cm^{-1}) of Ni-P.[31] More importantly, the E_{2g}^1 and A_{1g} vibrations of $1T_{0.72}$-MoS_2@NiS_2 at 382.2 and 408.1 cm^{-1} were red-shifted by 6.0 and 5.2 cm^{-1}, respectively (**Supplementary Fig. 4b**). Thus, NiS_2 nanoparticles are between the $1T_{0.41}$-MoS_2 layers. Similarly, the E_{2g}^1 and A_{1g} peaks for the $1T_{0.81}$-MoS_2@Ni_2P catalyst slightly red-shifted by 7.3 and 3.0 cm^{-1}, respectively. These results confirm that rich multi-heterojunction interface edges active sites catalysts were successfully synthesized.

Electronic structure characterizations of $1T_{0.72}$-MoS_2@NiS_2 and $1T_{0.81}$-MoS_2@Ni_2P catalysts. To further identify the surface electronic structure of multi-heterogeneous interface catalysts, we applied the high-resolution transmission electron microscopy (HRTEM) to assess the morphology and crystal structures of $1T_{0.81}$-MoS_2@Ni_2P and $1T_{0.72}$-MoS_2@NiS_2 catalysts. **Supplementary Fig. 5a, b** shows the typical low-magnification image of the $1T_{0.72}$-MoS_2@NiS_2 on the Cu grid, which confirms the flower-like nanosphere morphologies of $1T_{0.72}$-MoS_2@NiS_2. TEM and corresponding elemental distribution map obtained for the $1T_{0.72}$-MoS_2@NiS_2 sample demonstrated uniformly distributed Mo, Ni, and S (**Supplementary Fig. 5c-c_4**). As revealed by the HRTEM image (**Fig. 2a-c** and **Supplementary Fig. 5e, f**), NiS_2 nanoparticles are decorated on MoS_2 nano-sheets edge. The HRTEM of the $1T_{0.72}$-MoS_2@NiS_2 catalyst clearly shows the

crystal lattice of 0.25 nm, referring to the NiS_2 (210). Interestingly, **Fig. 2a** shows the HRTEM image of $1T_{0.72}$-MoS_2@NiS_2 flower-like nano-sheets, in which there demonstrates the lattice fringes perpendicularly to the electron beam direction circled by blood-color, justifying the S defect (**Fig. 2c**). The trigonal lattice in the yellow circle **(Fig. 2c**) implies the presence of 1T phase MoS_2, while the hexagonal lattice in the blue circle (**Fig. 2c**) suggests the presence of 2H phase MoS_2. The above-described results further confirm the successful preparation of the $1T_{0.72}$-MoS_2@NiS_2 multi-heterojunction interface catalyst. The anion is changed to be P to produce $1T_{0.81}$-MoS_2@Ni_2P multi-heterojunction interface catalyst by phosphorus vapor thermal treatment. **Supplementary Fig. 6a**, b displays the morphologies of $1T_{0.81}$-MoS_2@Ni_2P catalyst, overlapping nanosheets with many embedded particles can be clearly identified. There is an obvious alternation of 1T and 2H phases, and a large number of defects (**Fig. 2f**). As shown in **Supplementary Fig. 6c**, there are the distributions of Mo, Ni, S, and P over the whole $1T_{0.81}$-MoS_2@Ni_2P catalyst, verifying that Ni_2P nanoparticles are encapsulated by MoS_2 edges. The interplanar spacings, equal to 0.62 and 0.22 nm, match (002) and (111) interplanar distances of MoS_2 and Ni_2P, respectively (**Fig. 2d**, and **e**). Similarly, **Fig. 2e, f** displays two amplified HRTEM images truncated from **Fig. 2d**. **Fig. 2f** demonstrates some hexagonal and trigonal lattice areas of semi-conductor $2H_{phase}$- and metallic $1T_{phase}$-MoS_2, respectively. The HRTEM results further confirm the successful preparation of the $1T_{0.81}$-MoS_2@Ni_2P multi-heterojunction interface catalyst.

Next, we performed XPS measurement to assess the elemental valence states of all the as-synthesized samples (**Fig. 2g-i** and **Supplementary Fig. 7**). Full XPS spectrum for $1T_{0.72}$-MoS_2@NiS_2 electrode (**Supplementary Fig. 7a**) showed that atomic ratios of Mo, S and Ni were equal to 13.96%, 36.96% and 4.39 %, respectively, and close to that measured by HRTEM elemental mapping (~14.30 %, 35.87 %, and 4.76 %). Mo 3d spectra obtained for the multi-heterojunction interfaces of the $1T_{0.72}$-MoS_2@NiS_2, $1T_{0.81}$-MoS_2@Ni_2P, $1T_{0.41}$-MoS_2 and $2H_{phase}$-MoS_2 electrodes showed Mo $3d_{3/2}$ and $3d_{5/2}$ peaks of the 2H phase at 233.2 and 229.9 eV, and of the 1T phase at 232.4 and 229.1 eV in $1T_{0.72}$-MoS_2@NiS_2 and $1T_{0.81}$-MoS_2@Ni_2P, respectively. These results suggest Mo^{4+} presence (**Fig. 2g)**. Interestingly, the 1T phase contents in the $1T_{0.81}$-MoS_2@Ni_2P and $1T_{0.72}$-MoS_2@NiS_2 samples (equal to 81% and 72%, respectively) were higher than the 41% value observed for the $1T_{0.41}$-MoS_2 phase. Thus, phosphorus or sulfur implantation further facilitates the phase transformation of $1T_{phase}$-MoS_2.[22,27] The S 2p spectra also displayed similar results (**Fig. 2h**). All as-prepared electrodes also have two new doublet peaks of 161.9 eV and 163.2 eV, indicating that these belong to the characteristic peaks of $1T_{phase}$-MoS_2, further confirming 2H → 1T phase transformation.[22] Ni 2p spectrum showed peaks at 855.4 and 872.9 eV corresponding to Ni $2p_{1/2}$ and $2p_{3/2}$, respectively (**Fig. 2i)** and two satellite peaks, suggesting the existence of Ni^{2+} [32] in the $1T_{0.72}$-MoS_2@NiS_2 and $1T_{0.81}$-MoS_2@Ni_2P samples. Both peaks were slightly shifted (by 0.5 eV) towards higher binding energies, suggesting that there is an interaction between NiS_2 (or Ni_2P) and MoS_2 via as-formed hetero-structures. For the $1T_{0.81}$-MoS_2@Ni_2P catalyst, the XPS survey spectrum displays that the atomic ratio of Mo, S, P and Ni are 19.29%, 32.7%, 8.23%, 8.23% (**Supplementary Fig. 7a**). Also, as shown in **Supplementary Fig. 7b**, there are two doublets of P 2p peaks

(129.4 eV, 130.2 eV), which further confirms the formation of Ni_2P. These results indicate the successful synthesis of multi-heterogeneous-interface catalysts.

Electrocatalytic HER performances in alkaline and acidic media. $1T_{0.72}$-MoS_2@NiS_2 and $1T_{0.81}$-MoS_2@Ni_2P electrodes exhibited attractive multi-heterogeneous interface edges, plentiful active sites and abundant mass transfer and gas release channels and are expected to be used as very effective and stable catalysts for H_2 production. First, we analyzed HER activities (in 1.0 M KOH) of the electrodes containing these electrodes. The overpotentials of the electrodes containing $1T_{0.72}$-MoS_2@NiS_2 and $1T_{0.81}$-MoS_2@Ni_2P were 128 and 168 mV at 10 mA/cm^2, respectively (see linear sweep voltammetry (LSV) results in **Fig. 3a).** These values are close to the Pt/C electrode potential equal to 84 mV. For the reaction kinetics analysis, we adjusted the Tafel slopes of these electrodes using the Tafel equation [38,39] and obtained the smallest slopes equal to 68 and 79 mV/dec for the electrodes containing $1T_{0.72}$-MoS_2@NiS_2 and $1T_{0.81}$-MoS_2@Ni_2P, respectively (**Supplementary Fig. 8a**). These values are even closer to the corresponding slope of the Pt/C electrode (equal to 56 mV/dec). Thus, electrodes containing $1T_{0.72}$-MoS_2@NiS_2 and $1T_{0.81}$-MoS_2@Ni_2P as active materials exhibit the fastest HER processes and better reactivity, which is attributed to the multi-heterogeneous interface effect, a large number of defects, and a higher proportion of $1T_{phase}$-MoS_2. Next, we evaluated the long-term cycling stability of the as-prepared electrodes using the chronopotentiometry technique at 10 and 30 mA/cm^2, respectively. The electrodes containing $1T_{0.72}$-MoS_2@NiS_2 and $1T_{0.81}$-MoS_2@Ni_2P were very robust and exhibited negligible damping after 16 h measurement (**Supplementary Fig. 8b**), and the LSV curves measured before and after the long-term tests are almost the same (**Supplementary Fig. 8c**), demonstrating excellent long-term stability. **Supplementary Fig. 8d** lists the overpotential values for the 20.0 wt % Pt/C, $1T_{0.72}$-MoS_2@NiS_2 and $1T_{0.81}$-MoS_2@Ni_2P electrodes in 1.0 M KOH at various current densities. $1T_{0.72}$-MoS_2@NiS_2 electrodes exhibited lower overpotential. Generally, low overpotential and Tafel slope values demonstrated the superior HER catalytic activities, which was the case for our $1T_{0.72}$-MoS_2@NiS_2 and $1T_{0.81}$-MoS_2@Ni_2P electrodes. $1T_{0.72}$-MoS_2@NiS_2 containing electrode has such excellent HER activity comparable to those of as-reported Mo-based materials (**Fig. 3b**) and composites and various representative catalysts[25,26,28,31-34] (**Supplementary Table 1**). Thus, $1T_{0.72}$-MoS_2@NiS_2 electrode is a catalyst with the best HER activity in alkaline solutions.

To obtain the electrochemically active area (ECSA) of the $1T_{0.72}$-MoS_2@NiS_2 and $1T_{0.81}$-MoS_2@Ni_2P electrodes, the double-layer capacitance (C_{dl}) was calculated because the two values are proportional to each other. Therefore, we tested their cyclic voltammetry (CV) by continuously increasing scanning speed (**Supplementary Fig. 9a-c**) in order to obtain the CV curve of the electrode materials in the non-Faraday region (-0.2-0.4 V). Then, as shown in **Supplementary Fig. 9d**, the C_{dl} was calculated from the plot slope (slope = $2C_{dl}$) between current-density difference (Δj) (0.15 V vs. RHE) and scan rate. The $1T_{0.72}$-MoS_2@NiS_2 electrodes possessed the highest C_{dl} value (C_{dl} = 359.7 mF/cm^2), suggesting a multi-heterogeneous interface could be effectively enhanced conductivity and exposed more active sites of as-

prepared electrodes. We recorded the electrochemical impedance spectra (EIS). The corresponding Nyquist (**Supplementary Fig. 10)** of the $1T_{0.72}$-MoS_2@NiS_2 electrode showed the lowest value for the charge transfer resistance (R_{ct}). Thus, it possessed very favorable charge transfer kinetics.

Next, we also studied the HER performance of all the as-prepared electrodes in 0.5 M H_2SO_4 (**Fig. 3c).** The HER catalytic performance of the electrodes containing $1T_{0.81}$-MoS_2@Ni_2P and $1T_{0.72}$-MoS_2@NiS_2 were significantly improved their HER activities according to the LSV data: their overpotential values at 10 mA/cm^2 were as low as 38.9 and 98.5 mV, respectively, which is lower than the values for the electrodes containing $1T_{0.41}$-MoS_2@$Ni(OH)_2$ (236 mV), $1T_{0.41}$-MoS_2 (389 mV), $1T_{phase}$-MoS_2 (392 mV), and $2H_{phase}$-MoS_2 (354 mV). The Tafel slopes for the electrodes containing $1T_{0.81}$-MoS_2@Ni_2P and $1T_{0.72}$-MoS_2@NiS_2 were 41 and 42 mV/dec (**Supplementary Fig. 11a).** These values were lower than the values obtained for electrodes containing $1T_{0.41}$-MoS_2 (65 mV/dec), $1T_{phase}$-MoS_2 (76 mV/dec), and $2H_{phase}$-MoS_2 (71 mV/dec) and were close to the electrode based on 20 wt% Pt/C (38 mV/dec). It is probably because, in the acidic environment, the H_2 desorption is the limiting step because H^+ are abundant. The $1T_{0.81}$-MoS_2@Ni_2P electrode had a weaker adsorption capacity toward H_{ads} so it exhibits a better catalytic effect than $2H_{phase}$-MoS_2.[40] Meanwhile, compared to the other electrodes, $1T_{0.81}$-MoS_2@Ni_2P also has a higher ECSA because it has a larger C_{dl} (C_{dl} = 106.15 mF/cm^2, **Supplementary Fig. 12**) and, as a result, more catalytical sites, which significantly contributed to the overall activity. Furthermore, $1T_{0.81}$-MoS_2@Ni_2P also possesses a much smaller R_{ct}, in contrast to other electrodes at 50 mV overpotential vs. RHE (**Supplementary Fig. 13**), revealing satisfied electron transport and good catalytic kinetics, which leads to high activity and low Tafel slope. **Supplementary Fig. 11b** shows that at 10 and 45 mA/cm^2, $1T_{0.81}$-MoS_2@Ni_2P and $1T_{0.72}$-MoS_2@NiS_2 electrodes were very durable and possesses negligible damping after 16 h measurement, which displays excellent long-term stability. In addition, even after 16 h of a chronoamperometric stability test of the electrodes, the current density remains above 95% (**Supplementary Fig. 11c**), and there is only a slight deviation for the LSV recorded after the stability test, indicating that as-prepared electrodes have very good stability in an acidic environment. As to 20.0 wt % Pt/C, $1T_{0.72}$-MoS_2@NiS_2, and $1T_{0.81}$-MoS_2@Ni_2P electrodes in 0.5 M H_2SO_4, **Supplementary Fig. 11d** shows overpotentials vs. various current densities. $1T_{0.81}$-MoS_2@Ni_2P exhibits lower overpotential. We also compared the overpotentials (at 10 mA/cm^2 in acidic medium) and Tafel slopes with previously excellent Mo-based electrocatalysts[27,31,41-44] (**Fig. 3d** and **Supplementary Table 2).** Catalytic HER performance of $1T_{0.81}$-MoS_2@Ni_2P is also superior. Based on the above results, $1T_{0.81}$-MoS_2@Ni_2P multi-heterogeneous interface catalyst shows the remarkable intrinsic HER activities in acidic medium mainly attributed to multi-heterointerface interface edges active sites.

Theoretical calculation and mechanisms analysis of the surface electronic structure and HER activation energy for the as-prepared electrocatalysts. To explain the distinguished synergistic effect of $1T_{0.72}$-MoS_2@NiS_2 (or $1T_{0.81}$-MoS_2@Ni_2P) multi-heterogeneous interface catalysts, Density functional theory (DFT) calculations were also performed. Model building and computational parameters can be seen in

the "**Methods**" section. Firstly, the interfacial electron interaction was investigated. The charge difference images (**Fig. 4a, b** and **Supplementary Fig. 14**) reveal the charge transfer from $1T_{0.41}$-MoS_2 to the Ni_2S or/and Ni_2P interface, and the introduction of 1T phase is more conducive to charge transfer from MoS_2 to NiS_2 or Ni_2P interface, which significantly increase the interface electron concentration and thus improve its activity. To better understand the surface electronic structure reconfiguration of MoS_2 through coordinated phase transition and interface regulation in theory, the band structure and density of states (DOS) of bare NiS_2, Ni_2P, $2H_{phase}$-MoS_2, $1T_{phase}$-MoS_2, $2H_{phase}$-MoS_2@NiS_2, $2H_{phase}$-MoS_2@Ni_2P, $1T_{phase}$-MoS_2@NiS_2, and $1T_{phase}$-MoS_2@Ni_2P (**Fig. 4c-e** and **Supplementary Fig. 15**) obtained using the hybrid DFT-HSE06 exchange–correlation functional, which is presented in the Supplementary Information. The calculation results show that the bare NiS_2 exhibits typical semiconductor characteristics (**Fig. 4c**), with a narrow bandgap equal to 0.68 eV (**Supplementary Fig. 15a**). The band structure of $1T_{phase}$-MoS_2 (**Fig. 4d**) and $1T_{phase}$-MoS_2@NiS_2 (**Fig. 4e**) exhibited a certain zero bandgap, indicating a complete transition from the semiconductor phase (0.91 eV, **Supplementary Fig. 18b**) to the metallic phase (0 eV) with improved conductivities.[27] Notably, the intensity of PDOS of $1T_{phase}$-MoS_2@NiS_2 was higher than that of $1T_{phase}$-MoS_2 and NiS_2 at the Fermi level (**Supplementary Fig. 15**). Thus, the electron mobility of the $1T_{phase}$-MoS_2@NiS_2 catalysts was more favorable for the efficient charge transfer, which agrees consistent with the EIS test results.[45] Moreover, the PDOS results imply that the NiS_2 interface hybrid generates some new interface electronic states in $1T_{phase}$-MoS_2 (**Supplementary Fig. 15c**), which was very likely because of hybridization of the d-orbital of Mo and an empty d-orbital of Ni. Thus, higher HER activity of $1T_{phase}$-MoS_2@NiS_2 in comparison to $1T_{phase}$-MoS_2 agrees with the Fermi level DOS (**Fig. 4d. e**). Thus, the actual electrochemical performance would show even faster conductivity and charge transfer kinetics.

The HER effect was mainly studied by a three-state diagram containing original H^+ and intermediate H* states and 1/2 H_2 formation [30,46]. However, the energy of the intermediate state H*(ΔG_{H^*}) is a critical indicator of the ability of hydrogen evolution.[47] To reveal further the relationship of HER activity of catalysts with phase structure and heterojunction-interface, we used DFT to calculate the ΔG_{H^*} for HER on $2H_{phase}$-MoS_2, $1T_{phase}$-MoS_2, $2H_{phase}$-MoS_2@NiS_2, $2H_{phase}$-MoS_2@Ni_2P, $1T_{phase}$-MoS_2@NiS_2, and $1T_{phase}$-MoS_2@Ni_2P catalysts with partially multi-heterojunction interface modification. **Fig. 4f** displays the calculated free energy diagram on the most stable energy of the 2H phase, 1T phase, $2H_{phase}$-MoS_2@Ni_2P, $2H_{phase}$-MoS_2@NiS_2, $1T_{phase}$-MoS_2@NiS_2 and $1T_{phase}$-MoS_2@Ni_2P catalysts (**Supplementary Fig. 15**). For $2H_{phase}$-MoS_2, the ΔG_{H^*} is very positive (1.18 eV), indicating that there is a strong interaction between H* and $2H_{phase}$-MoS_2, showing poor HER reaction kinetics. The introduction of the 1T-phase into MoS_2 can obviously increase the value of ΔG_{H^*} to – 0.36 eV, implying promoted HER activity compared to $2H_{phase}$-MoS_2. However, constructing multi-heterointerface interface edges active sites with NiS_2 ($1T_{phase}$-MoS_2@NiS_2) would lead to the ΔG_{H^*} value equal to almost 0 eV (- 0.17 eV). For comparison, ΔG_{H^*} for the $2H_{phase}$-MoS_2@NiS_2 was equal to 0.74 eV. The reason is that H* adsorbed on the surface of $2H_{phase}$-MoS_2 bounds to Mo atoms, and strong Mo-H strength and poor conductivity.

However, H* can be absorbed not only by the $1T_{phase}$-MoS_2@NiS_2 surface. Ni atoms possess empty d orbitals capable of binding H atoms, thereby weakening the Mo-H strength. More importantly, the introduction of the 1T-phase not only increases its electrical conductivity but also creates abundant active sites at the multi-heterojunction interface edges, which synergistically promote HER activity (**Fig. 4g**). Thus, our work demonstrates a novel and efficient design to create multi-heterogeneous interfacial electrocatalysts without noble metal materials and with excellent HER activity.

Discussion

In summary, we have constructed multi-heterogeneous-interface catalysts ($1T_{0.81}$-MoS_2@Ni_2P and $1T_{0.72}$-MoS_2@NiS_2) by tuning its electronic structure of phase modulation synergistic with interfacial chemistry and defects to phosphorus or sulfur implantation strategies, which is an efficient approach to obtain abundant reactive sites of long-cycling and stable electrocatalysts for HER in alkaline and acidic surroundings. The as-achieved $1T_{0.81}$-MoS_2@Ni_2P and $1T_{0.72}$-MoS_2@NiS_2 electrodes only require small overpotentials of 38.9 (or 186) and 98.5 (or 128) mV to drive HER at 10 mA/cm^2 and have low Tafel slopes: 41 (or 79) and 42 (or 68) mV/dec in 0.5 M H_2SO_4 (or 1.0 M KOH). Accordingly, these results show varieties of multi-heterogeneous interfaces in $1T_{0.81}$-MoS_2@Ni_2P and $1T_{0.72}$-MoS_2@NiS_2 electrodes, which can be considered versatile electroactive sites and facilitate electron transfer because of their unique heterogeneous-effects. DFT calculation results also display that the introduction of metallic-phase MoS_2 and intrinsic HER-active Ni-based materials can regulate MoS_2 electronic structure effectively (a narrower bandgap and reduced Ni supply empty d-orbitals to facilitate H atom capture) and decrease Mo-H strength of $1T_{0.81}$-MoS_2@Ni_2P (or $1T_{0.72}$-MoS_2@NiS_2) catalysts that account for the outstanding HER properties with lower Tafel slopes and overpotentials compared with $2H_{phase}$-MoS_2, $1T_{phase}$-MoS_2 counterparts and other Mo-based catalysts. Thus, our work provides a new horizon for rationally designing multi-heterogeneous interfaces of non-precious electrocatalysts to realize excellent HER activities.

Methods

Synthesis of $1T_{0.41}$-MoS_2

MoS_2 microspheres were grown on carbon cloth (CC) hydrothermally. First, a CC (2 × 4 cm) was cleaned (for 15 min) using acetone and then sonicated in deionized water and ethanol for 10 minutes. Then, sodium molybdate ($Na_2MoO_4 \cdot 2H_2O$, 411.9 mg) and thiourea ($CS(NH_2)_2$, 608.96 mg) were added to deionized water (40 mL) and citric acid (20 mL). The mixture was magnetically stirred to form a cleaning solution, then placed into a 100 mL Teflon-lined autoclave and held in it at 180 °C for 12 h. Finally, the CC substrates with $1T_{0.41}$-MoS_2 microspheres (denoted through the paper as $1T_{0.41}$-MoS_2) were rinsed using deionized water and ethanol and vacuum-dried for 6 h at 60 ^oC. For comparison, deionized water was

used as the solvent, and $2H_{phase}$-MoS_2 microspheres were synthesized hydrothermally at 220 ^oC for 24 h from the same precursors.

Synthesis of $1T_{phase}$-MoS_2

We used Li-intercalated bulk MoS_2 to prepare $1T_{phase}$-MoS_2.[48] In an Ar-filled glove box, bulk MoS_2 (1.0 g) prepared by stripping were dispersed in 15 mL of 2M n-BuLi/hexane solution and stirred at ambient conditions for 48 h. The resulting black materials were repeatedly rinsed with anhydrous n-hexane and then centrifuged to eliminate n-butyl lithium excess and other solution impurities. The $1T_{phase}$-MoS_2 powder was prepared and was then coated on the CC substrate.

Synthesis of $1T_{0.41}$-MoS2@$Ni(OH)_2$

We use a standard three-electrode system to prepare $1T_{0.41}$-MoS_2@$Ni(OH)_2$. $1T_{0.41}$-MoS_2 acted as a working electrode, while Pt sheet and Ag/AgCl/3.5 M KCl acted as counter and reference electrodes. $Ni(OH)_2$ was electrodeposited on the $1T_{0.41}$-MoS_2 using 0.1 M $Ni(NO_3)_2$ at 5.0 mA/cm^2 cathode current density applied for 300 s. $1T_{0.41}$-MoS_2@$Ni(OH)_2$ samples were rinsed with deionized water and ethanol several times and vacuum-dried at 60 ^oC.

Synthesis of $1T_{0.72}$-MoS_2@NiS_2

The $1T_{0.72}$-MoS_2@NiS_2 multi-heterogeneous interfaces were prepared by the solid-vapor reaction method. First, a piece of $1T_{0.41}$-MoS_2@Ni(OH) grew on CC was put into the quartz tube with 32.0 mg S powder and was then sealed. Secondly, the quartz tube was positioned inside a tube furnace and was calcinated at 500 ^oC for 60 min to obtain a $1T_{0.72}$-MoS_2@NiS_2 electrode.

Synthesis of $1T_{0.81}$-MoS_2@Ni_2P

Similarly, the $1T_{0.81}$-MoS_2@Ni_2P multi-heterogeneous interfaces were also obtained by the solid-vapor reaction method. First, a piece of $1T_{0.41}$-MoS_2@$Ni(OH)_2$ grew on CC was put into the quartz tube with 31.0 mg red phosphorus and was then sealed. Secondly, the quartz tube was also calcinated at 580 ^oC for 1.0 h to prepare the $1T_{0.81}$-MoS_2@Ni_2P electrode. Additionally, 20 wt% Pt/C was also coated on CC substrate (2.0 mg/cm^2) and was labeled as 20% Pt/C for comparison.

Materials characterization

All as-synthetized electrodes were characterized by XRD (performed by Bruker D8 Advance instrument) and Raman spectroscopy (performed using Horiba LabRAB HR800 instrument). The sample morphologies were studied using SEM performed by Hitachi SU8010 instrument and TEM (performed by FEI Tecnai F30 instrument). XPS spectra were collected by the r ESCALAB 250Xi instrument manufactured by Thermo Fisher) using Al Kα radiation.

Electrochemical measurements

The loadings of $1T_{0.72}$-MoS_2@NiS_2 and $1T_{0.81}$-MoS_2@Ni_2P electrodes were 0.685 and 0.762 mg/cm^2, respectively. The tests were conducted by a three-electrode system containing 1.0 M KOH or 0.5 M H_2SO_4 electrolytes using a CHI 660E workstation. All materials were used as the working electrodes (1 × 1 cm in size) as-synthesized. A graphite rod and Hg/HgO or Ag/AgCl acted as the counter and reference electrodes, respectively. The LSV scan rate was 5.0 mV/s. CV tests were performed 50.0 mV/s scan rate. N_2 was passed through the electrolyte for 16 min) before each test to minimize the dissolved O_2 content.

DFT theoretical calculation

Model Building: According to the HRTEM micrographs, $1T_{phase}$-MoS_2, $2H_{phase}$-MoS_2, Ni_2P, and NiS_2 formed a multiphase heterojunction. $1T_{phase}$-MoS_2@Ni_2P interface, $1T_{phase}$-MoS_2@NiS_2 interface, $2H_{phase}$-MoS_2@Ni_2P interface, $2H_{phase}$-MoS_2@NiS_2 interface, bulk $1T_{phase}$-MoS_2, $2H_{phase}$-MoS_2 were also constructed as comparisons. Considering the Van der Waals forces between the two phases, the unrelaxed heterojunction interface distance was set to 3.0 Å. These original structures were obtained from *Materials Project Database*.[49]

Computational parameters: DFT calculation was applied to calculate electronic structures of two crystal structures by the partial augmented plane wave method (PAW) implemented in the VASP[50] using VASPKIT code for post-processing. Considering the heterojunction structure, the long-range force correction was considered by using the DFT-D3 correction method of Grimme.[51] The Perdew-Burke-Ernzerhof (PBE) generalized gradient approximation [52] was implemented for exchange-correlation energy calculations using 550 eV kinetic energy cut off for the plane-wave basis. Then structural optimizations using a conjugate gradient (CG) method based on the pre-optimized structure were repeated until the maximum force component on each atom remained below 0.01 eV/Å. Monkhorst-Pack k-point meshes in the first Brillouin zone of the primitive cell were used the VASPKIT code recommended accuracy levels of 0.04 for the optimization calculation and 0.02 for the static calculation, respectively. After fully relaxing the structures, one final (electronic scf) step with the tetrahedron method using Blöchl corrections and denser k-meshes was employed for DOS calculation. In addition to the H adsorbed energy calculations, the frequency calculation of free H and free energy correction at 298.15 K (including the entropy and zero-point energy contributions) were also calculated. To avoid abnormal entropy contribution, frequencies less than 50 cm^{-1} are set to be 50 cm^{-1}.

Declarations

Competing interests

The authors declare no competing interests.

Author contributions

M. Liu and J. Wang contributed equally to this work. G. -G Wang and Y. Yang supervised the project. M. Liu conducted electrocatalysts growth, characterization experiments and electrochemical test; J. Wang conducted theoretical calculation section; F. Li, Y. Cai and F. Zhang discussed the results and helped the preparation of figures; M. Liu, J. Wang, G. -G Wang and Y. Yang assessed the data and wrote the paper taking into account feedback from all authors. Also, we thank Yuting Luo for the helpful discussions.

Acknowledgements

This work was supported by Science Foundation of Science Foundation of the National Key Laboratory of Science and Technology on Advanced Composites in Special Environments (Grant No. 6142905192507), Shenzhen Science and Technology Plan Supported Project (Grant No. JCYJ20170413105844696), China Scholarship Council (Grant No. 201606125092),the National Key R&D Project from Minister of Science and Technology in China (No. 2016YFA0202701), the University of Chinese Academy of Sciences (Grant No. Y8540XX2D2), the National Natural Science Foundation of China (No. 52072041), External Cooperation Program of BIC, Chinese Academy of Sciences (No. 121411KYS820150028), the 2015 Annual Beijing Talents Fund (No. 2015000021223ZK32), and Qingdao National Laboratory for Marine Science and Technology (No. 2017ASKJ01).

Data availability

All experimental data can be supplied upon request.

References

1. Choi, W. et al. High-detectivity multilayer MoS_2 phototransistors with spectral response from ultraviolet to infrared. Adv. Mater. **24**, 5832-5836 (2012).
2. Shi, J. et al. Two-dimensional metallic tantalum disulfide as a hydrogen evolution catalyst. Nat. Commun. **8**, 958 (2017).
3. Yang, L. et al. Combining photocatalytic hydrogen generation and capsule storage in graphene based sandwich structures. Nat. Commun. **8**, 16049 (2017).
4. Yi, J. et al. Large-scale production of ultrathin carbon nitride-based photocatalysts for high-yield hydrogen evolution Appl. Catal. B: Environ. **281**, 119475 (2021).
5. Wei, Z. et al. Simultaneous realization of sulfur-rich surface and amorphous nanocluster of NiS_{1+x} cocatalyst for efficient photocatalytic H_2 evolution. Appl. Catal. B: Environ. **280**, 119455 (2021).
6. Peng, L. et al. Accelerated alkaline hydrogen evolution on $M(OH)_x$/M-$MoPO_x$ (M = Ni, Co, Fe, Mn) electrocatalysts by coupling water dissociation and hydrogen ad-desorption steps. Chem. Sci. **11**, 2487-2493 (2020).
7. Wang, P. et al. Precise tuning in platinum-nickel/nickel sulfide interface nanowires for synergistic hydrogen evolution catalysis. Nat. Commun. **8**, 14580 (2017).

8. Chen, Y. et al. Electrocatalytically inactive SnS_2 promotes water adsorption/dissociation on molybdenum dichalcogenides for accelerated alkaline hydrogen evolution. Nano Energy **64**, 103918 (2019).
9. Mahmood, N. et al. Electrocatalysts for hydrogen evolution in alkaline electrolytes: mechanisms, challenges, and prospective solutions. Adv. Sci. **5**, 1700464 (2018).
10. Sun, Y. et al. Strongly coupled dual zerovalent nonmetal doped nickel phosphide nanoparticles/nitrogen, boron-graphene hybrid for pH-universal hydrogen evolution catalysis. Appl. Catal. B: Environ. **278**, 119284 (2020).
11. Walter, M. et al. Solar Water Splitting Cells. Chem. Rev. **110**, 6446 (2010).
12. Yang, B. et al. Amorphous phosphatized ruthenium-iron bimetallic nanoclusters with Pt-like activity for hydrogen evolution reaction. Appl. Catal. B: Environ. **283**, 119583 (2021).
13. Gao, B. et al. 3D flower-like defected MoS_2 magnetron-sputtered on candle soot for enhanced hydrogen evolution reaction. Appl. Catal. B: Environ. **263**, 117750 (2020).
14. Ren, J. et al. Molybdenum-based nanoparticles (Mo_2C, MoP and MoS_2) coupled heteroatoms-doped carbon nanosheets for efficient hydrogen evolution reaction. Appl. Catal. B: Environ. **263**, 118352 (2020).
15. Yao, N. et al. Oxygen-Vacancy-Induced CeO_2/Co_4N heterostructures toward enhanced pH-Universal hydrogen evolution reactions. Appl. Catal. B: Environ. **277**, 119282 (2020).
16. Fan, H. et al. Plasma-heteroatom-doped Ni-V-Fe trimetallic phospho-nitride as high-performance bifunctional electrocatalyst. Appl. Catal. B: Environ, **268**, 118440 (2020).
17. Wang, H. et al. Confined growth of pyridinic N–Mo_2C sites on MXenes for hydrogen evolution. J. Mater. Chem. A. **8**, 7109-7116 (2020).
18. Zhang, X. et al. Structure and phase regulation in MoxC (α-MoC_{1-x}/β-Mo_2C) to enhance hydrogen evolution. Appl. Catal. B: Environ. **247**, 78-85 (2019).
19. Ge, Y. et al. Transforming nickel hydroxide into 3D prussian blue analogue array to obtain Ni_2P/Fe_2P for efficient hydrogen evolution reaction. Adv. Energy Mater. **8**, 1800484 (2018).
20. Xu, K. et al. Yin-Yang Harmony: Metal and nonmetal dual-doping boosts electrocatalytic activity for alkaline hydrogen evolution. ACS Energy Lett. **3**, 2750-2756 (2018).
21. Anjum, M.A.R. et al. Efficient Hydrogen Evolution Reaction Catalysis in Alkaline Media by All-in-One MoS_2 with Multifunctional Active Sites. Adv. Mater. **30**, 1707105 (2018).
22. Chang, K. et al. Targeted Synthesis of 2H- and 1T-Phase MoS_2 Monolayers for Catalytic Hydrogen Evolution. Adv. Mater. **28**, 10033-10041 (2016).
23. Kim, M. et al. Covalent 0D–2D heterostructuring of Co_9S_8–MoS_2 for enhanced hydrogen evolution in all pH electrolytes. Adv. Funct. Mater. **30**, 2002536 (2020).
24. Liu, Z. et al. Vertical nanosheet array of 1T phase MoS_2 for efficient and stable hydrogen evolution. Appl. Catal. B: Environ. **246**, 296-302 (2019).

25. Lei, C. et al. Efficient alkaline hydrogen evolution on atomically dispersed Ni–N_x Species anchored porous carbon with embedded Ni nanoparticles by accelerating water dissociation kinetics. Energy Environ. Sci. **12**, 149-156 (2019).
26. Wang, S. et al. Ultrastable In-Plane 1T–2H MoS_2 heterostructures for enhanced hydrogen evolution reaction. Adv. Energy Mater. **8**, 1801345 (2018).
27. Deng, S. et al. Synergistic doping and intercalation: realizing deep phase modulation on MoS_2 arrays for high-efficiency hydrogen evolution reaction. Angew. Chem. **58**, 16289-16296 (2019).
28. Chen, W. et al. Achieving rich and active alkaline hydrogen evolution heterostructures via interface engineering on 2D 1T-MoS_2 quantum sheets. Adv. Funct. Mater. **30**, 2000551 (2020).
29. Luo, Y. et al. Morphology and surface chemistry engineering toward pH-universal catalysts for hydrogen evolution at high current density. Nat. Commun. **10**, 269 (2019).
30. Zhang, B. et al. Interface engineering: the $Ni(OH)_2/MoS_2$ heterostructure for highly efficient alkaline hydrogen evolution. Nano Energy **37**, 74-80 (2017).
31. Kim, M. et al. Activating MoS_2 basal plane with Ni_2P nanoparticles for Pt-Like hydrogen evolution reaction in acidic media. Adv. Funct. Mater. **29**, 1809151 (2019).
32. Lin, J. et al. Defect-rich heterogeneous MoS_2/NiS_2 nanosheets electrocatalysts for efficient overall water splitting. Adv. Sci. **6**, 1900246 (2019).
33. Jia, Y. et al. A heterostructure coupling of exfoliated Ni–Fe hydroxide nanosheet and defective graphene as a bifunctional electrocatalyst for overall water splitting. Adv. Mater. 29, 1700017 (2017).
34. Liu, Y. et al. Interface engineering of (Ni, Fe)S_2@ MoS_2 heterostructures for synergetic electrochemical water splitting. Appl. Catal. B: Environ. **247**, 107-114 (2019).
35. Liu, Z. et al. Heterogeneous nanostructure based on 1T-phase MoS_2 for enhanced electrocatalytic hydrogen evolution. ACS Appl. Mater. Inter. **9**, 25291-25297 (2017).
36. Ding, W. et al. Highly ambient-stable 1T-MoS_2 and 1T-WS_2 by hydrothermal synthesis under high magnetic fields. ACS Nano **13**, 1694-1702 (2019).
37. Wang, X. et al. 2D/2D 1T-MoS_2/Ti_3C_2 MXene heterostructure with excellent supercapacitor performance. Adv. Funct. Mater. 30, 0190302 (2020).
38. Chang, B. et al. Bimetallic NiMoN nanowires with a preferential reactive facet: an ultraefficient bifunctional electrocatalyst for overall water splitting. Chem. Sus. Chem. **11**, 3198–3207 (2018).
39. Zhang, J. et al. Synergistic interlayer and defect engineering in VS_2 nanosheets toward efficient electrocatalytic hydrogen evolution reaction. Small **14**, 1703098 (2018).
40. Deng, J. et al. Enhanced electron penetration through an ultrathin graphene layer for highly efficient catalysis of the hydrogen evolution reaction. Angew. Chem. Int. Ed. **54**, 2100–2104 (2015).
41. Jiao, Y. et al. Porous plate-like MoP assembly as an efficient pH-universal hydrogen evolution electrocatalyst. ACS Appl. Mater. Inter. **12**, 49596–49606 (2020).

42. Mishra, I.K. et al. Hierarchical CoP/Ni_5P_4/CoP microsheet arrays as a robust pH-universal electrocatalyst for efficient hydrogen generation. Energy Environ. Sci. **11**, 2246-2252 (2018).
43. Li, H. et al. Activating and optimizing MoS_2 basal planes for hydrogen evolution through the formation of strained sulphur vacancies. Nat. Mater. **15**, 48-53 (2016).
44. Chen, Y. et al. Electrocatalytically inactive SnS_2 promotes water adsorption/dissociation on molybdenum dichalcogenides for accelerated alkaline hydrogen evolution. Nano Energy **64**, 103918 (2019).
45. Zhang, B. et al. Simultaneous interfacial chemistry and inner Helmholtz plane regulation for superior alkaline hydrogen evolution. Energy Environ. Sci. **13**, 3007-3013 (2020).
46. Zhang, J. et al. Engineering water dissociation sites in MoS_2 nanosheets for accelerated electrocatalytic hydrogen production. Energy Environ. Sci. **9**, 2789-2793 (2016).
47. Wu, Y. et al. Electron density modulation of $NiCo_2S_4$ nanowires by nitrogen incorporation for highly efficient hydrogen evolution catalysis. Nat. Commun. **9**, 1425 (2018).
48. Luo, Y. et al. Two-Dimensional MoS_2 Confined $Co(OH)_2$ Electrocatalysts for Hydrogen Evolution in Alkaline Electrolytes. ACS Nano **12**, 4565–4573 (2018)
49. Jong, M. et al. Charting the complete elastic properties of inorganic crystalline compounds. Sci. Data. **2**, 150009 (2015).
50. Intan, N. et al. Ab initio modeling of transition metal dissolution from the $LiNi_{0.5}Mn_{1.5}O_4$ cathode ACS Appl. Mater. Inter. **11**, 20110-20116 (2019).
51. Grimme, S. et al. Effect of the damping function in dispersion corrected density functional theory. J. Comput. Chem. **32**, 1456-1465 (2011).
52. Perdew, J. et al. Generalized gradient approximation made simple. Phys. Rev. Lett. **78**, 1396-1396 (1997).

Figures

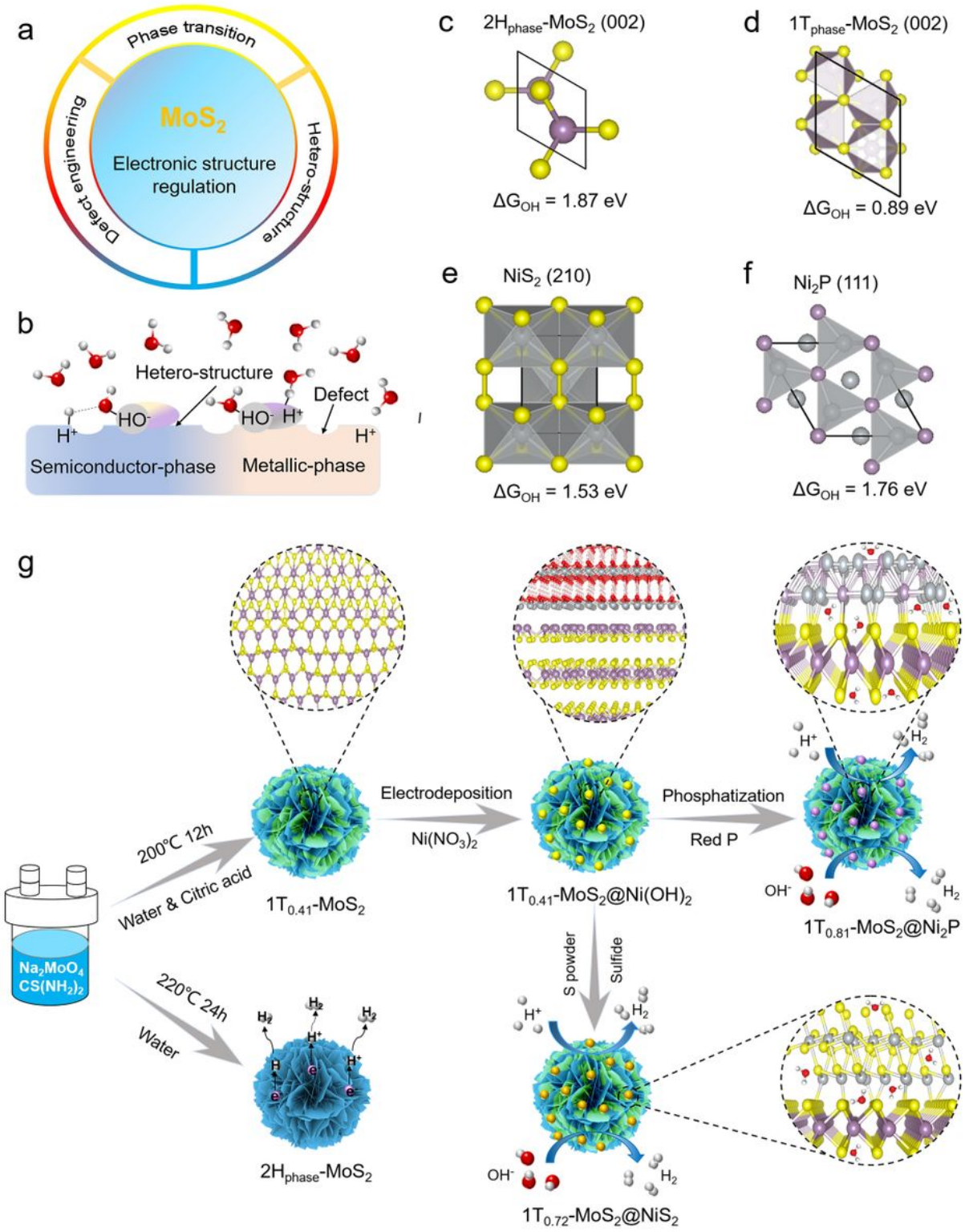

Figure 1

Motivation and design of electrocatalyst. a Tuning strategy of the electronic structure of the MoS2 surface. b Design ideas of hydrogen evolution catalyst. c-f the energetics of hydroxyl species on 2Hphase-MoS2 (002), 1Tphase-MoS2 (002), NiS2 (210), and Ni2P (111) HER electrocatalyst surfaces. g Schematics of the 1T0.72-MoS2@NiS2 and 1T0.81-MoS2@Ni2P synthesis steps.

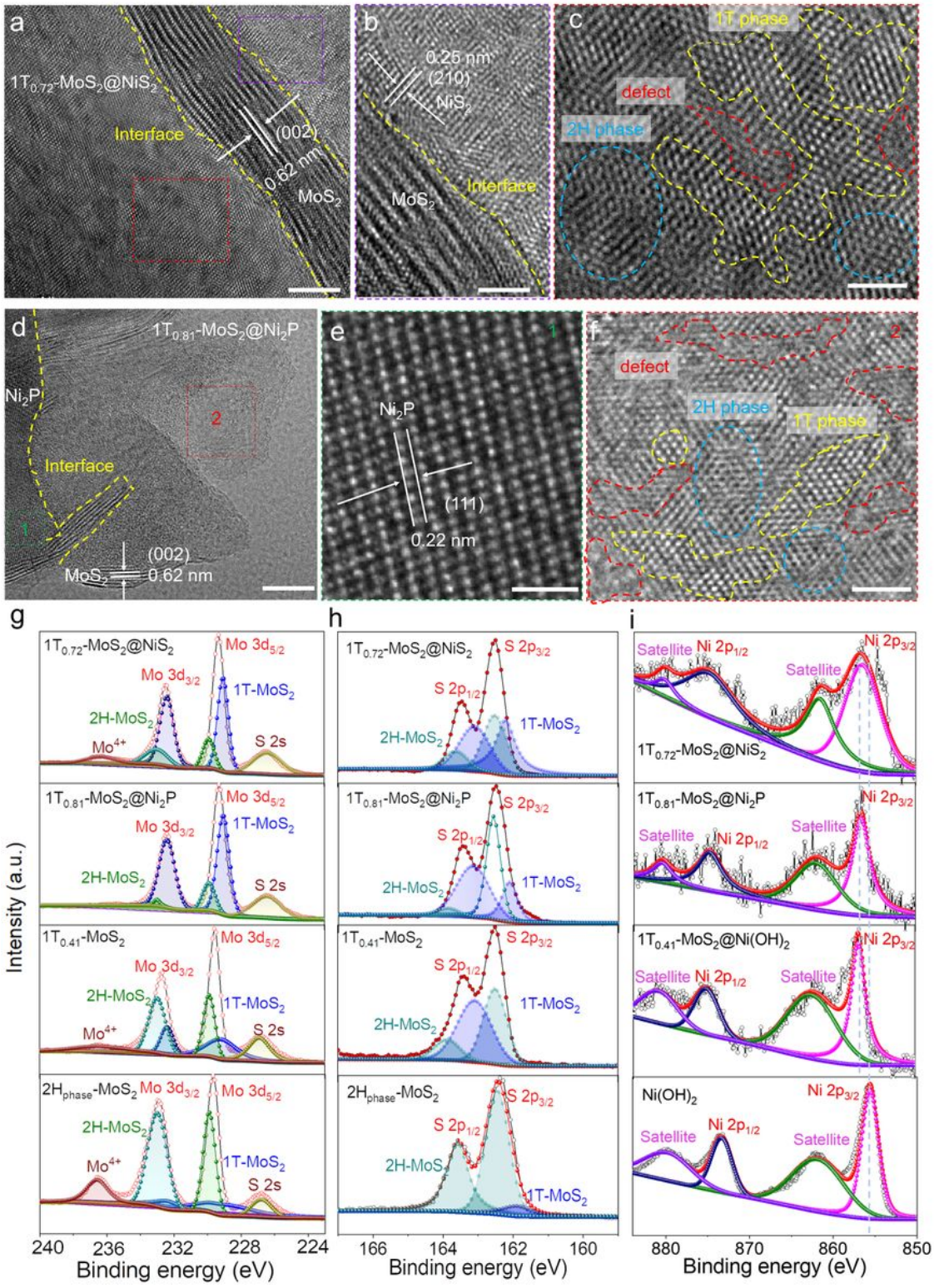

Figure 2

Electronic structure characterizations of 1T0.72-MoS2@NiS2 and 1T0.81-MoS2@Ni2P catalysts. a-c HRTEM image of 1T0.72-MoS2@NiS2. (b) shows NiS2 lattice. (c) shows 2H and 1T lattices. Scale bars are 5 nm (a), 1 nm (b), and 2 nm (c). d-f Typical HR-TEM image of 1T0.81-MoS2@Ni2P. (g) shows Ni2P lattice fringes. (h) shows 2H and 1T lattices. Scale bars are 5 nm (f), 1 nm (g) and 2 nm (h). g HR Mo 3d core-level XPS spectra of 1T0.72-MoS2@NiS2, 1T0.81-MoS2@Ni2P, 1T0.41-MoS2 and 2Hphase-MoS2. h

S 2p core-level XPS spectra of 1T0.72-MoS2@NiS2, 1T0.81-MoS2@Ni2P, 1T0.41-MoS2 and 2Hphase-MoS2, respectively. i Ni 2p XPS spectrum for 1T0.72-MoS2@NiS2, 1T0.81-MoS2@Ni2P, 1T0.41-MoS2@Ni(OH)2, and Ni(OH)2.

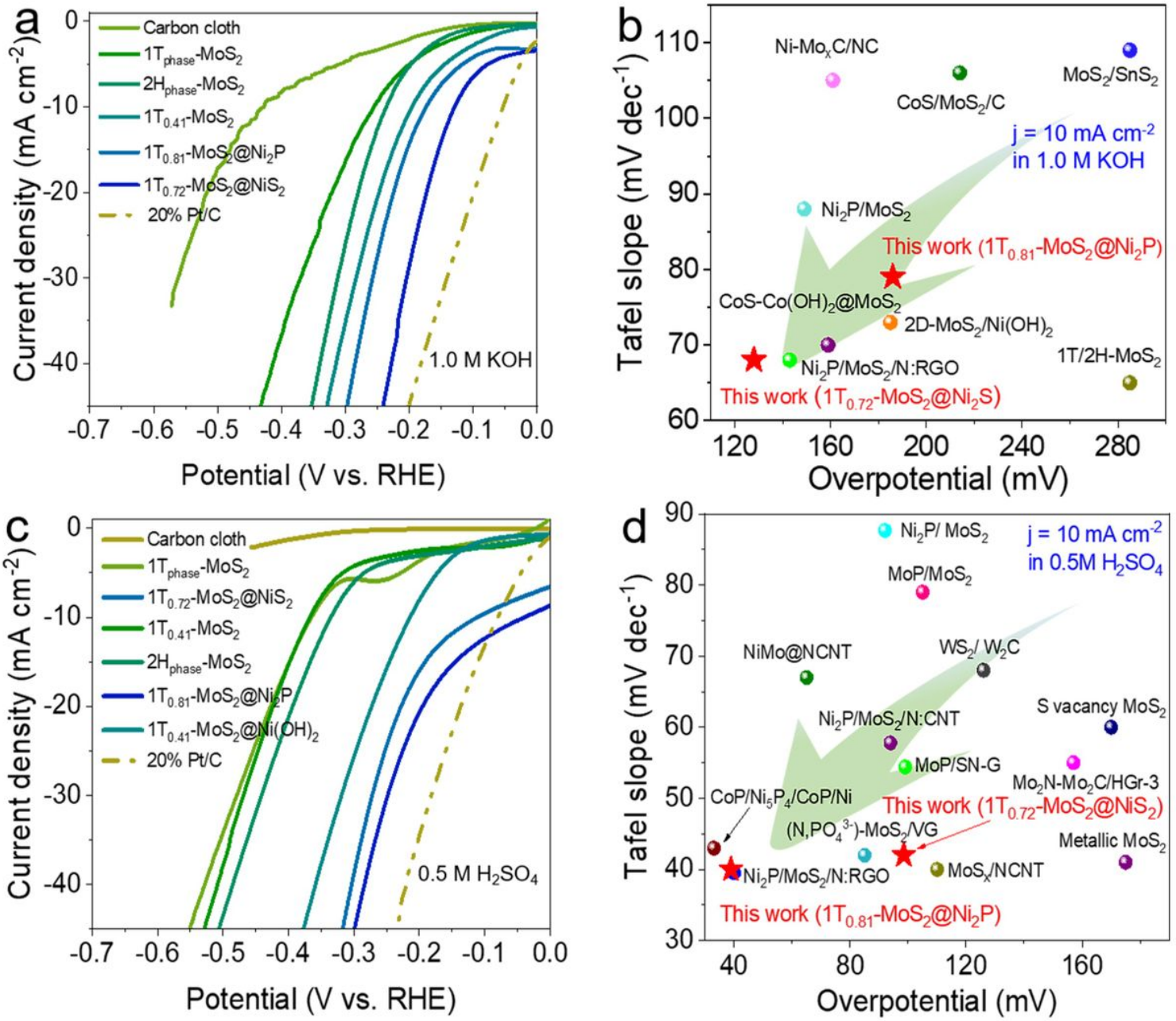

Figure 3

HER performed in alkaline and acidic electrolytes. a LSV curves in 1M KOH. b η10 and Tafel slopes for various Mo-based HER electrocatalysts in 1.0 M KOH. c. LSV curves in 0.5 M H2SO4. d. η10 and Tafel slopes for various Mo-based HER catalysts in 0.5 M H2SO4.

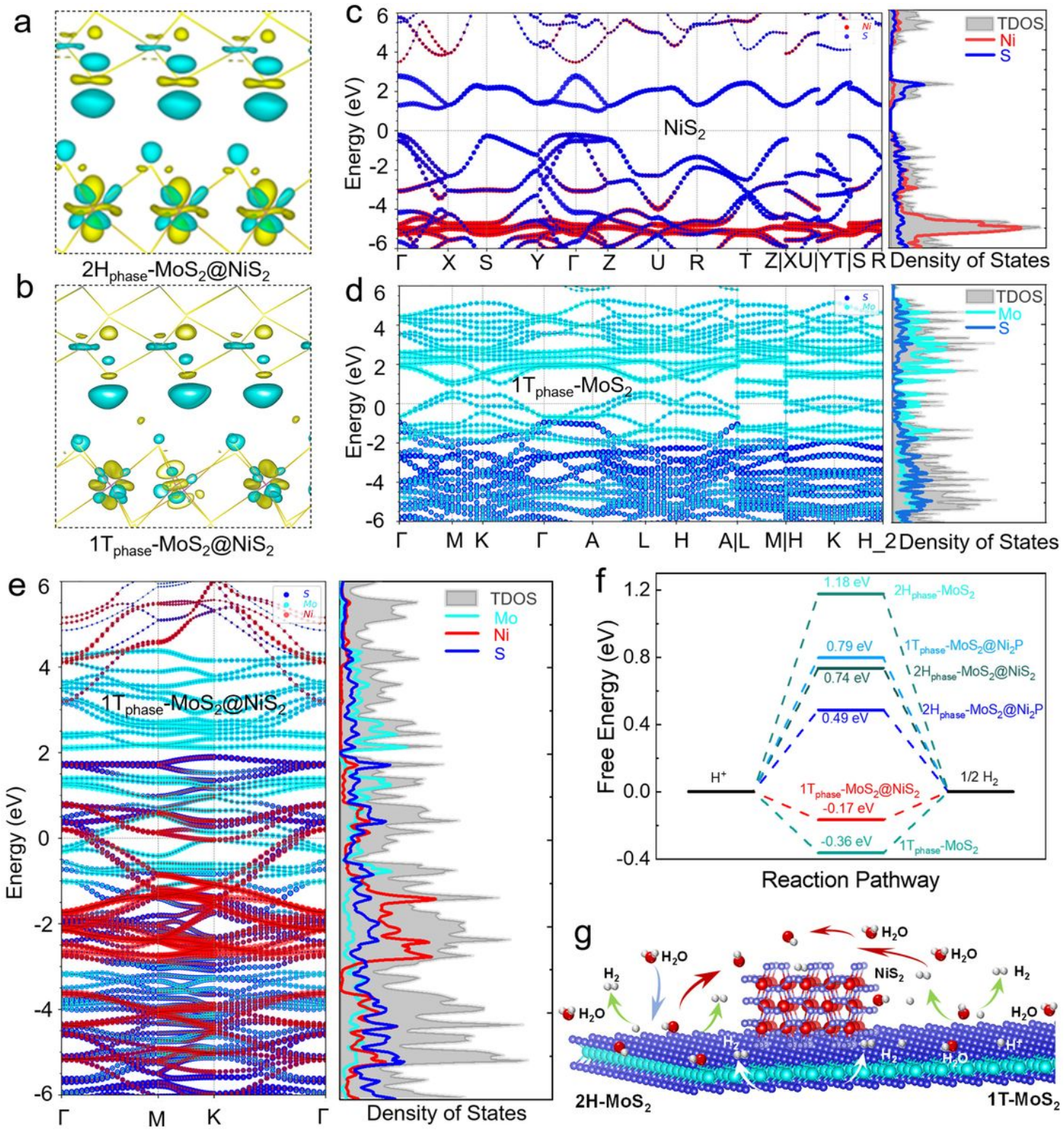

Figure 4

Theoretical calculation and mechanisms analysis of the surface structure and HER activation energy of the as-prepared electrocatalysts. a, b the deformation of the electronic density of 2Hphase-MoS2@NiS2 and 1Tphase-MoS2@NiS2 interface, in which yellow/green isosurfaces correspond to positive/negative spin densities (0.00295308 e/Å3). Band structure and density of states (DOS) for NiS2 (c), 1Tphase-MoS2 (d) and 1Tphase-MoS2@NiS2 (e). f Free-energy diagrams of H2 adsorption by the 2Hphase-MoS2,

1Tphase-MoS2, 2Hphase-MoS2@Ni2P, 2Hphase-MoS2@NiS2, 1Tphase-MoS2@NiS2 and 1Tphase-MoS2@Ni2P. g Schematics showing water activation, *H intermediate formation and hydrogen generation on multi-heterojunction interface electrocatalysts.

Supplementary Files

This is a list of supplementary files associated with this preprint. Click to download.

- Supplementaryinformation.doc